DeepBedMap: Using a deep neural network to better resolve the bed topography of Antarctica

Wei Ji Leong[1] and Huw Joseph Horgan[1]

[1]Antarctic Research Centre, Victoria University of Wellington, Wellington, New Zealand

Correspondence: W. J. Leong (weiji.leong@vuw.ac.nz)

Abstract. To better resolve the bed elevation of Antarctica, we present DeepBedMap - a novel machine learning method that produces realistic Antarctic bed topography from multiple remote sensing data inputs. Our super-resolution deep convolutional neural network model is trained on scattered regions in Antarctica where high resolution (250 m) groundtruth bed elevation grids are available. The model is then used to generate high resolution bed topography in less well surveyed areas. DeepBedMap

5   improves on previous interpolation methods by not restricting itself to a low spatial resolution (1000 m) BEDMAP2 raster image as its prior. It takes in additional high spatial resolution datasets, such as ice surface elevation, velocity and snow accumulation to better inform the bed topography even in the absence of ice-thickness data from direct ice-penetrating radar surveys. Our DeepBedMap model is based on an adapted Enhanced Super Resolution Generative Adversarial Network architecture, chosen to minimize per-pixel elevation errors while producing realistic topography. The final product is a four times

10 upsampled (250 m) bed elevation model of Antarctica that can be used by glaciologists interested in the subglacial terrain, and by ice sheet modellers wanting to run catchment or continent-scale ice sheet model simulations. We show that DeepBedMap offers a more realistic topographic roughness profile compared to a standard bicubic interpolated BEDMAP2 and BedMachine Antarctica, and envision it to be used where a high resolution bed elevation model is required.

1 Introduction

15 The bed of the Antarctic ice sheets is one of the most challenging surfaces on Earth to map due to the thick layer of ice cover. Knowledge of bed elevation is however essential for estimating the volume of ice currently stored in the ice sheets, and for input to the numerical models that are used to estimate the contribution ice sheets are to likely to make to sea level in the coming century. The Antarctic ice sheet is estimated to hold a sea level equivalent (SLE) of 57.9 ± 0.9 m (Morlighem et al.,

20 2019). Between 2012 and 2017, the Antarctic Ice Sheet was losing mass at an average rate of 219 ± 43 Gt yr^{-1} (0.61 ± 0.12 mm yr^{-1} SLE), with most of the ice loss attributed to the acceleration, retreat and rapid thinning of major West Antarctic Ice Sheet outlet glaciers (The IMBIE team, 2018). Bed elevation exerts additional controls on ice flow by routing subglacial water, and providing frictional resistance to flow (Siegert et al., 2004). Bed roughness, especially at short-wavelengths, exerts

a frictional force against the flow of ice, making it an important influence on ice velocity (Bingham et al., 2017; Falcini
25 et al., 2018). The importance of bed elevation has led to major efforts to compile bed elevation models of Antarctica, notably
with the BEDMAP1 (Lythe and Vaughan, 2001) and BEDMAP2 (Fretwell et al., 2013) products. A need for higher spatial
resolution Digital Elevation Model (DEM) is also apparent, as ice sheet models move to using sub-kilometer grids in order to
quantify glacier ice flow dynamics more accurately (Graham et al., 2017). Finer grids are especially important at the ice sheet's
grounding zone where adaptive mesh refinement schemes have focused on (e.g. Cornford et al., 2016), and attention to the
30 bed roughness component is imperative for proper modelling of fast flowing outlet glaciers (Durand et al., 2011; Nias et al.,
2016). Here we address the challenge of producing a high resolution DEM while preserving a realistic representation of the
bed terrain's roughness.

Estimating bed elevation directly from geophysical observations primarily uses ice penetrating radar methods (e.g. Robin
et al., 1970). Airborne radar methods enable reliable along track estimates with low uncertainty (around the 1% level) intro-
35 duced by imperfect knowledge of the firn and ice velocity structure, with some potential uncertainty introduced by picking the
bed return. Radar derived bed estimates remain limited in their geographic coverage (Fretwell et al., 2013), and are typically
anisotropic in their coverage, with higher spatial sampling in the along track direction than between tracks.

To overcome these limitations, indirect methods of estimating bed elevation have been developed, which use surface obser-
vations combined with glaciological process knowledge to determine ice thickness (e.g. van Pelt et al., 2013). A non-linear
40 relationship exists between the thickness of glaciers, ice streams and ice sheets and how they flow (Raymond and Gudmunds-
son, 2005), meaning one can theoretically use a well resolved surface to infer bed properties (e.g. Farinotti et al., 2009). Using
surface observation inputs, such as the glacier outline, surface digital elevation models, surface mass balance, surface rate of
elevation change, and surface ice flow velocity, various models have been tested in the Ice Thickness Models Intercomparison
eXperiment (ITMIX, Farinotti et al., 2017) to determine ice thickness (surface elevation minus bed elevation). While signifi-
45 cant inter-model uncertainties do exist, they can be mitigated by combining several models in an ensemble to provide a better
consensus estimate (Farinotti et al., 2019). On a larger scale, the inverse technique has also been applied to the Greenland
(Morlighem et al., 2017) and Antarctic (Morlighem et al., 2019) ice sheets, specifically using the mass conservation approach
(Morlighem et al., 2011).

We present a deep neural network method that belongs to the inverse modelling category and is trained on direct ice-
50 penetrating radar observations over Antarctica. An artificial neural network, loosely based on biological neural networks, is a
system made up of neurons. Each neuron comprises of a simple mathematical function that takes an input to produce an output
value, and neural networks work by combining many of these neurons together. The term deep neural network is used when
there is not a direct function mapping between the input data and final output, but two or more layers that are connected to
one another (see LeCun et al., 2015, for a review). They are trained using backpropagation, a procedure whereby the weights
55 or parameters of the neurons' connections are adjusted, so as to minimize the error between the groundtruth and output of
the neural network (Rumelhart et al., 1986). Similar work has been done before using artificial neural networks for estimating
bed topography (e.g. Clarke et al., 2009; Monnier and Zhu, 2018), but to our knowledge, none so far in the glaciological
community have attempted to use convolutional neural networks that works in a more spatially-aware, 2-dimensional setting.

Convolutional neural networks differ from standard artificial neural networks in that they use kernels or filters in place of
60 regular neurons (again, see LeCun et al., 2015, for a review). The techniques we employ are prevalent in the computer vision
community, having existed since the 1980s (Fukushima and Miyake, 1982; LeCun et al., 1989) and are commonly used in visual
pattern recognition tasks (e.g. Lecun et al., 1998; Krizhevsky et al., 2012). Our main contributions are twofold: 1) Present a
high resolution (250 m) bed elevation map of Antarctica that goes beyond the 1 km resolution of BEDMAP2 (Fretwell et al.,
2013); 2) Design a deep convolutional neural network to integrate as many remote sensing datasets as possible which are
65 relevant for estimating Antarctica's bed topography. We name the neural network "DeepBedMap", and the resulting digital
elevation model (DEM) product as "DeepBedMap_DEM".

2   Related Work

2.1   Super-Resolution

Super-Resolution involves the processing of a low resolution raster image into a higher resolution one (Tsai and Huang,
70 1984). The idea is similar to the work on enhancing regular photographs to look crisper. The problem is especially ill-posed
because a specific low resolution input can correspond to many possible high resolution outputs, resulting in the development of
several different algorithms aimed at solving this challenge (see Nasrollahi and Moeslund, 2014, for a review). One promising
approach is to use deep neural networks (LeCun et al., 2015) to learn an end-to-end mapping between the low and high
resolution images, a method coined Super-Resolution Convolutional Neural Network (SRCNN, Dong et al., 2014). Since the
75 development of SRCNN, multiple advances have been made to improve the perceptual quality of super resolution neural
networks (see Yang et al., 2018, for a review). One way is to use a better loss function, also known as a cost function. A loss
function is a mathematical function that represents the error between the output of the neural network and the groundtruth
(see also Appendix A). By having an adversarial component in its loss function, the Super-Resolution Generative Adversarial
Network (SRGAN, Ledig et al., 2016) manages to produce super resolution images with finer perceptual details. A Generative
80 Adversarial Network (Goodfellow et al., 2014) consists of two neural networks, a Generator and a Discriminator. A common
analogy used is to treat the Generator as an artist that produces imitation paintings, and the Discriminator as an art critic that
determines the authenticity of the paintings. The artist wants to fool the critic into believing its paintings are real, while the
critic tries to identify problems with the painting. Over time, the artist or generator model learns to improve itself based on
the critic's judgement, producing authentic looking paintings with high perceptual quality. Perceptual quality is the extent to
85 which an image looks like a valid natural image, usually as judged by a human. In this case, perceptual quality is quantified
mathematically by the Discriminator or critic taking into account high level features of an image like contrast, texture, etc.
Another way to improve performance is by reconfiguring the neural network's architecture, wherein the layout or building
blocks of the neural network are changed. By removing unnecessary model components and adding residual connections (He
et al., 2015), the Enhanced Deep Super-Resolution network (EDSR, Lim et al., 2017) features a deeper neural network model
90 that has better performance than older models. For the DeepBedMap model, we choose to adapt an Enhanced Super-Resolution
Generative Adversarial Network (ESRGAN, Wang et al., 2018) that brings together the ideas mentioned above. This approach

produces state of the art perceptual quality and won the 2018 Perceptual Image Restoration and Manipulation Challenge on Super-Resolution (Third Region) (Blau et al., 2018).

2.2 Network Conditioning

95 Network conditioning means having a neural network process one source of information in the context of other sources (Dumoulin et al., 2018). In a geographic context, conditioning is akin to using not just one layer, but also other relevant layers with meaningful links to provide additional information to the task at hand. Many ways exist to insert extra conditional information into a neural network, such as concatenation-based conditioning, conditional biasing, conditional scaling, and conditional affine transformations (Dumoulin et al., 2018). We choose to use the concatenation-based conditioning approach, whereby

100 all of the individual raster images are concatenated together channel-wise, much like the individual bands of a multispectral satellite image. This was deemed the most appropriate conditioning method as all the contextual remote sensing datasets are raster grid images, and also because this approach aligns with related work in the remote sensing field.

An example similar to this DEM super-resolution problem is the classic problem of pan-sharpening, whereby a blurry low resolution multispectral image conditioned with a high resolution panchromatic image can be turned into a high resolution

105 multispectral image. There is ongoing research into the use of deep convolutional neural networks for pan-sharpening (Masi et al., 2016; Scarpa et al., 2018), sometimes with the incorporation of specific domain-knowledge (Yang et al., 2017), all of which show promising improvements over classical image processing methods. More recently, generative adversarial networks (Goodfellow et al., 2014) have been used in the conditional sense for general image-to-image translation tasks (e.g. Isola et al., 2016; Park et al., 2019), and also for producing more realistic pan-sharpened satellite images (Liu et al., 2018). Our

110 DeepBedMap model builds upon these ideas and other related DEM super-resolution work (Xu et al., 2015; Chen et al., 2016), while incorporating extra conditional information specific to the cryospheric domain for resolving the bed elevation of Antarctica.

3 Data and Methods

3.1 Data Preparation

115 Our convolutional neural network model works on 2D images, so we have to ensure all the datasets are in a suitable raster grid format. Groundtruth bed elevation points picked from radar surveys (see Table 1) are first compiled together onto a common Antarctic Stereographic Projection (EPSG:3031) using the WGS84 datum, reprojecting where necessary. These points are then gridded onto a 250 m spatial resolution (pixel-node registered) grid. We preprocess the points first using Generic Mapping Tools v6.0 (GMT6, Wessel et al., 2019), computing the median elevation for each pixel block in a regular grid. The preprocessed

120 points are then run through an adjustable tension continuous curvature spline function with a tension factor set to 0.35 to produce a digital elevation model grid. This grid is further post-processed to mask out pixels that are more than 3 pixels (750 m) from the nearest groundtruth point.

Table 1. High Resolution groundtruth datasets from ice-penetrating radar surveys (collectively labelled as y) used to train the DeepBedMap model. Training site locations can be seen in Figure 2.

Location	Citation
Pine Island Glacier	Bingham et al. (2017)
Wilkes Subglacial Basin	Jordan et al. (2010)
Carlson Inlet	King (2011)
Rutford Ice Stream	King et al. (2016)
Various locations in Antarctica	Shi et al. (2010)

Table 2. Remote Sensing dataset inputs into the DeepBedMap neural network model.

Symbol	Name	Variable	Spatial Resolution	Citation
x	BEDMAP2	bed elevation (m)	1000 m	Fretwell et al. (2013)
w^1	REMA	surface elevation (m)	100 m**	Howat et al. (2018)
w^2	MEaSUREs Ice Velocity	VX,VY (m yr^{-1})*	500 m***	Mouginot et al. (2019a)
w^3	Antarctic Snow Accumulation	snow accumulation rate (kg m^{-2} a^{-1})	1000 m	Arthern et al. (2006)

* note that the x and y components of velocity are used here instead of the norm.

** gaps in 100 m mosaic filled in with bilinear resampled 200 m resolution REMA image.

*** originally 450 m, bilinear resampled to 500 m.

To create the training dataset, we use a sliding window to obtain square tiles cropped from the high resolution (250 m) groundtruth bed elevation grids, with each tile required to be completely filled with data (i.e. no NaN values). Besides these groundtruth bed elevation tiles, we also obtain other tiled inputs (see Table 2) corresponding to the same spatial bounding box area. To reduce border edge artifacts in the prediction, the neural network model's input convolutional layers (see Figure 1) use no padding (also known as 'valid' padding) when performing the initial convolution operation. This means that the model input grids (x, w^1, w^2, w^3) have to cover a larger spatial area than the groundtruth grids (y). More specifically, the model inputs cover an area of 11x11 km (e.g. 11x11 pixels for BEDMAP2) while the groundtruth grids cover an area of 9x9 km (36x36 pixels). As the pixels of the groundtruth grids may not align perfectly with that of the model's input grids, we use bilinear interpolation to ensure that all the input grids cover the same spatial bounds as that of the reference groundtruth tiles. The general location of these training tiles are shown as orange boxes in Figure 2.

3.2 Model Design

Our DeepBedMap model is a Generative Adversarial Network (Goodfellow et al., 2014) composed of two convolutional neural network models, a Generator G_θ that produces the bed elevation prediction, and a Discriminator D_η critic that will judge the quality of this output. The two models are trained to compete against each other, with the Generator trying to produce

images that are misclassified as real by the Discriminator, and the Discriminator learning to spot problems with the Generator's prediction in relation to the groundtruth. Following this is a mathematical definition of the neural network models and their architecture.

140   The objective of the main super-resolution Generator model G_θ is to produce a high resolution (250 m) grid of Antarctica's bed elevation $\hat{y}$ given a low resolution (1000 m) BEDMAP2 (Fretwell et al., 2013) image x. However, the information contained in BEDMAP2 is insufficient for this regular super-resolution task, so we provide the neural network with more context through network conditioning (see Section 2.2). Specifically, the model is conditioned at the input block stage with three raster grids (see Table 2): 1) ice surface elevation w^1, 2) ice surface velocity w^2, and 3) snow accumulation w^3. This can be formulated as

145   follows:

$$\hat{y} = G_\theta(x, w^1, w^2, w^3) \tag{1}$$

where G_θ is the Generator (see Figure 1) that produces high resolution image candidates $\hat{y}$. For brevity in the following equations, we simplify Equation (1) to hide conditional inputs w^1, w^2, w^3, so that all input images are represented using x. To train the Generative Adversarial Network, we update the parameters of the Generator θ and Discriminator η as follows:

$$150 \quad \hat{\theta} = \arg\min_\theta \frac{1}{N} \sum_{n=1}^{N} L_G(\hat{y}_n, y_n) \tag{2}$$

$$\hat{\eta} = \arg\min_\eta \frac{1}{N} \sum_{n=1}^{N} L_D(\hat{y}_n, y_n) \tag{3}$$

where new estimates of the parameters $\hat{\theta}$ and $\hat{\eta}$ are produced by minimizing the total loss functions L_G and L_D respectively for the Generator G and Discriminator D. $\hat{y}_n, y_n$ are the set of predicted and groundtruth high resolution images over N training samples. The generator network's loss L_G is a custom perceptual loss function with four weighted components - content,

155   adversarial, topographic and structural loss. The discriminator network's loss L_D is designed to maximize the likelihood that predicted images are classified as fake (0) and groundtruth images are classified as real (1). Details of these loss functions are described in Appendix A.

     Noting that the objective of the Generator G is opposite to that of the Discriminator D, we formulate the adversarial min-max problem following Goodfellow et al. (2014) as so:

$$160 \quad \min_G \max_D V(G, D) = \mathbb{E}_{y \sim P_{\text{data}}(y)}[\ln D(y)] + \mathbb{E}_{x \sim P_{G(x)}}[\ln(1 - D(G(x)))] \tag{4}$$

where for the Discriminator D, we maximize the expectation $\mathbb{E}$, or the likelihood that the probability distribution of the Discriminator's output fits $D(y) = 1$ when $y \sim P_{\text{data}}(y)$, i.e. we want the Discriminator to classify the high resolution image as real (1) when the image y is in the distribution of the groundtruth images $P_{\text{data}}(y)$. For the Generator G, we minimize

the likelihood that the Discriminator classifies the Generator output $D(G(x)) = 0$ when $x \sim P_{G(x)}$, i.e. we do not want the

165   Discriminator to classify the super resolution image as fake (0) when the inputs x is in the distribution of generated images $P_{G(x)}$. The overall goal of the entire network is to make the distribution of generated images $G(x)$ as similar as possible to the groundtruth y through optimizing the value function V.
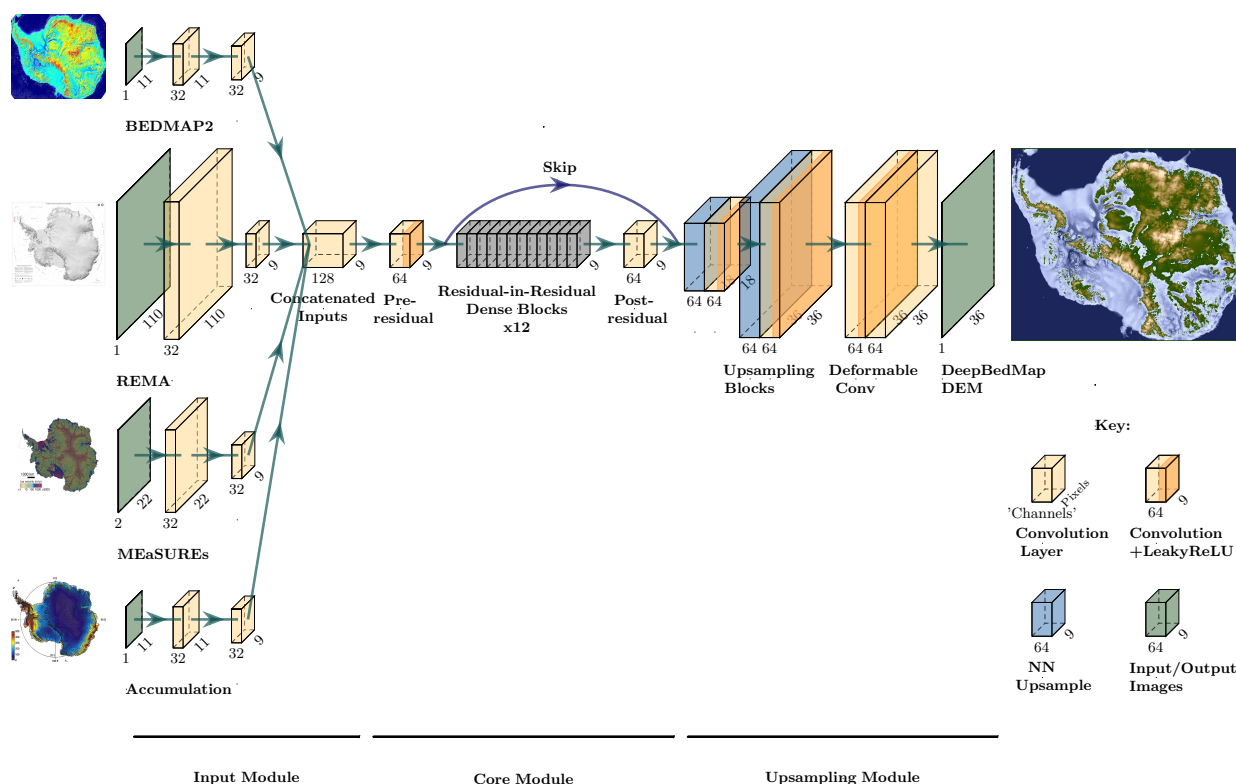
Figure 1. DeepBedMap Generator model architecture composed of three modules. The input module processes each of the four inputs (see Table 2) into a consistent tensor. The core module processes the rich information contained within the concatenated inputs. The upsampling module scales the tensor up by four times and does some extra processing to produce the output DeepBedMap_DEM.

     DeepBedMap's model architecture is adapted from the Enhanced Super Resolution Generative Adversarial Network (ESR-GAN, Wang et al., 2018). The Generator model G (see Figure 1) consists of an input, core, and upsampling module. The input

170   module is made up of four sub-networks, each one composed of a convolutional neural network that processes the input image into a consistent 9x9 shaped tensor. Note that the MEaSUREs Ice Velocity (Mouginot et al., 2019b) input has two channels, one each for the x and y velocity components. All the processed inputs are then concatenated together channel-wise before being fed into the core module. The core module is based on the ESRGAN architecture with 12 Residual-in-Residual Dense Blocks (see Wang et al., 2018, for details), saddled in between a pre-residual and post-residual convolutional layer. A skip connec-

175   tion runs from the pre-residual layer's output to the post-residual layer's output before being fed into the upsampling module.

This skip connection (He et al., 2016) helps with the neural network training process by allowing the model to also consider minimally processed information from the input module, instead of solely relying on derived information from the residual block layers when performing the upsampling. The upsampling module is composed of two upsampling blocks, specifically a nearest neighbour upsampling followed by a convolutional layer and Leaky Rectified Linear Unit (LeakyReLU, Maas et al.,
180   2013) activation, that progressively scales the tensors by 2x each time. Following this are two Deformable Convolutional layers (Dai et al., 2017) which produces the final output super resolution DeepBedMap_DEM. This Generator model is trained to gradually improve its prediction by comparing the predicted output with groundtruth images in the training regions (see Figure 2), using the total loss function defined in Equation (A9).

The main differences between the DeepBedMap Generator model and ESRGAN are the custom input block at the begin-
185   ning, and the Deformable Convolutional layers at the end. The custom input block is designed to handle the prior low resolution BEDMAP2 image and conditional inputs (see Table 2). Deformable Convolution was chosen in place of the standard Convolution so as to enhance the model's predictive capability by having it learn dense spatial transformations.

Besides the Generator model, there is a separate adversarial Discriminator model D (not shown in paper). Again, we follow ESRGAN's (Wang et al., 2018) lead by implementing the adversarial Discriminator network in the style of the Visual Geometry
190   Group convolutional neural network model (VGG, Simonyan and Zisserman, 2014). The Discriminator model consists of 10 blocks made up of a Convolutional, Batch Normalization (Ioffe and Szegedy, 2015) and LeakyReLU (Maas et al., 2013) layer, followed by two fully-connected layers comprised of 100 and 1 neurons respectively. For numerical stability, we omit the final fully-connected layer's sigmoid activation function from the Discriminator model's construction, integrating it instead into the binary cross entropy loss functions at Equation (A2) and Equation (A3) using the log-sum-exp function. The output of this
195   Discriminator model is a value ranging from 0 (fake) to 1 (real) that scores the Generator model's output image. This score is used by both the Discriminator and Generator in the training process, and helps to push the predictions towards more realistic bed elevations. More details of the neural network training setup can be found in Appendix B.

4   Results

4.1   DeepBedMap_DEM Topography

200   Here we present the output Digital Elevation Model (DEM) of the super-resolution DeepBedMap neural network model, and compare it with bed topography produced by other methods. The resulting DEM has a 250 m spatial resolution, therefore a four-times upsampled bed elevation grid product of BEDMAP2 (Fretwell et al., 2013). In Figure 2, we show that the full Antarctic-wide DeepBedMap_DEM manages to capture general topographical features across the whole continent. The model is only valid for grounded ice regions, but we have produced predictions extending outside of the grounding zone area (including ice
205   shelf cavities) using the same bed elevation, surface elevation, ice velocity and snow accumulation inputs where such data is available up to the ice shelf front. The predicted bed elevation under ice shelves is only intended to be used for visualization purposes. Alternatively, areas of DeepBedMap_DEM extending beyond the grounding zone can be cut out and replaced with other bathymetry grid products, using interpolation to smooth out the edges.
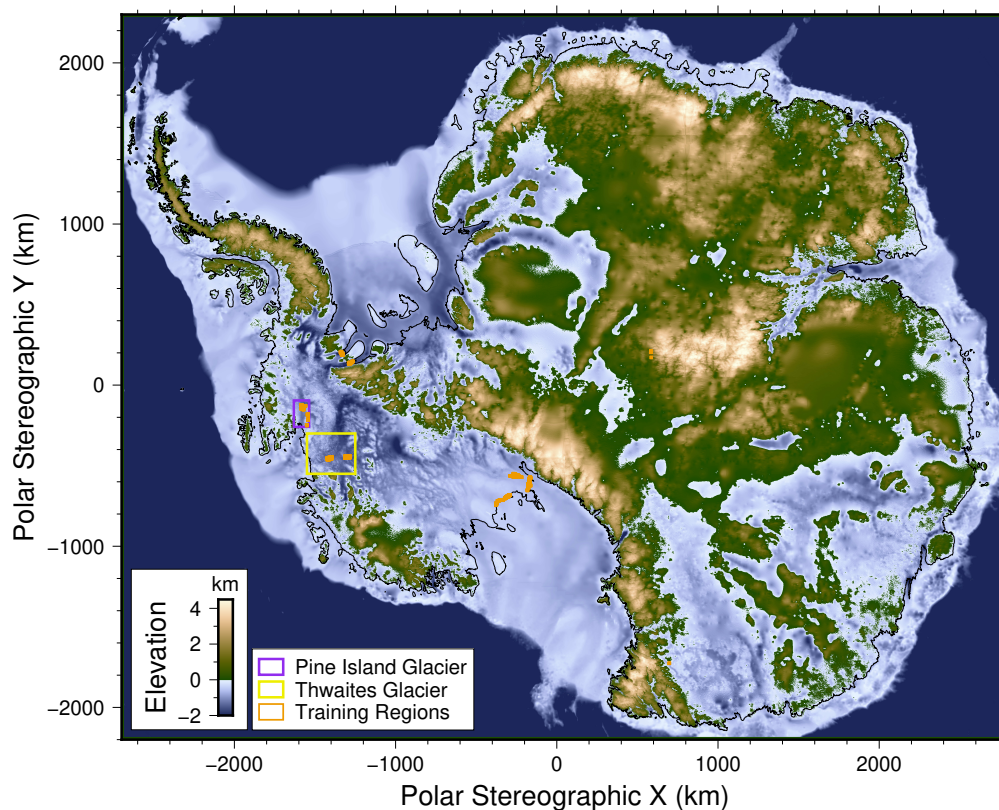
Figure 2. DeepBedMap_DEM over the entire Antarctic continent. Plotted on an Antarctic Stereographic Projection (EPSG:3031) with elevation referenced to the WGS84 datum. Grounding line is plotted as thin black line. Purple box shows Pine Island Glacier extent used in Figure 3. Yellow box shows Thwaites Glacier extent used in Figure 5. Orange areas show locations of training tiles (see Table 1).

We now highlight some qualitative observations of DeepBedMap_DEM's bed topography beneath Pine Island Glacier (Fig-
210 ure 3) and other parts of Antarctica (Figure 4). DeepBedMap_DEM shows a terrain with realistic topographical features, having
fine-scale bumps and troughs that makes it rougher than that of BEDMAP2 (Fretwell et al., 2013) and BedMachine Antarctica
(Morlighem, 2019) while still preserving the general topography of the area (Figure 3). Over steep topographical areas such
as the Transantarctic Mountains (Figure 4a, 4h), DeepBedMap produced speckle (**S**) texture patterns. Along fast flowing ice
streams and glaciers (Figure 4b, 4c, 4d, 4e, 4f, 4g, 4h), we can see ridges (**R**) aligned parallel to the sides of the valley, i.e.
215 along flow. In some cases, the ridges are also oriented perpendicular to the flow direction such at Whillans Ice Stream (Figure
4b), Bindschadler Ice Stream (Figure 4c) and Totten Glacier (Figure 4g), resulting in intersecting ridges that creates a box-like,
honeycomb structure. Over relatively flat regions in both West and East Antarctica (e.g. Figure 4g), there are some hummocky,
wave-like (**W**) patterns occasionally represented in the terrain. Terrace (**T**) features can occasionally be found winding along
the side of hills such as at the Gamburtsev Subglacial Mountains (Figure 4i).
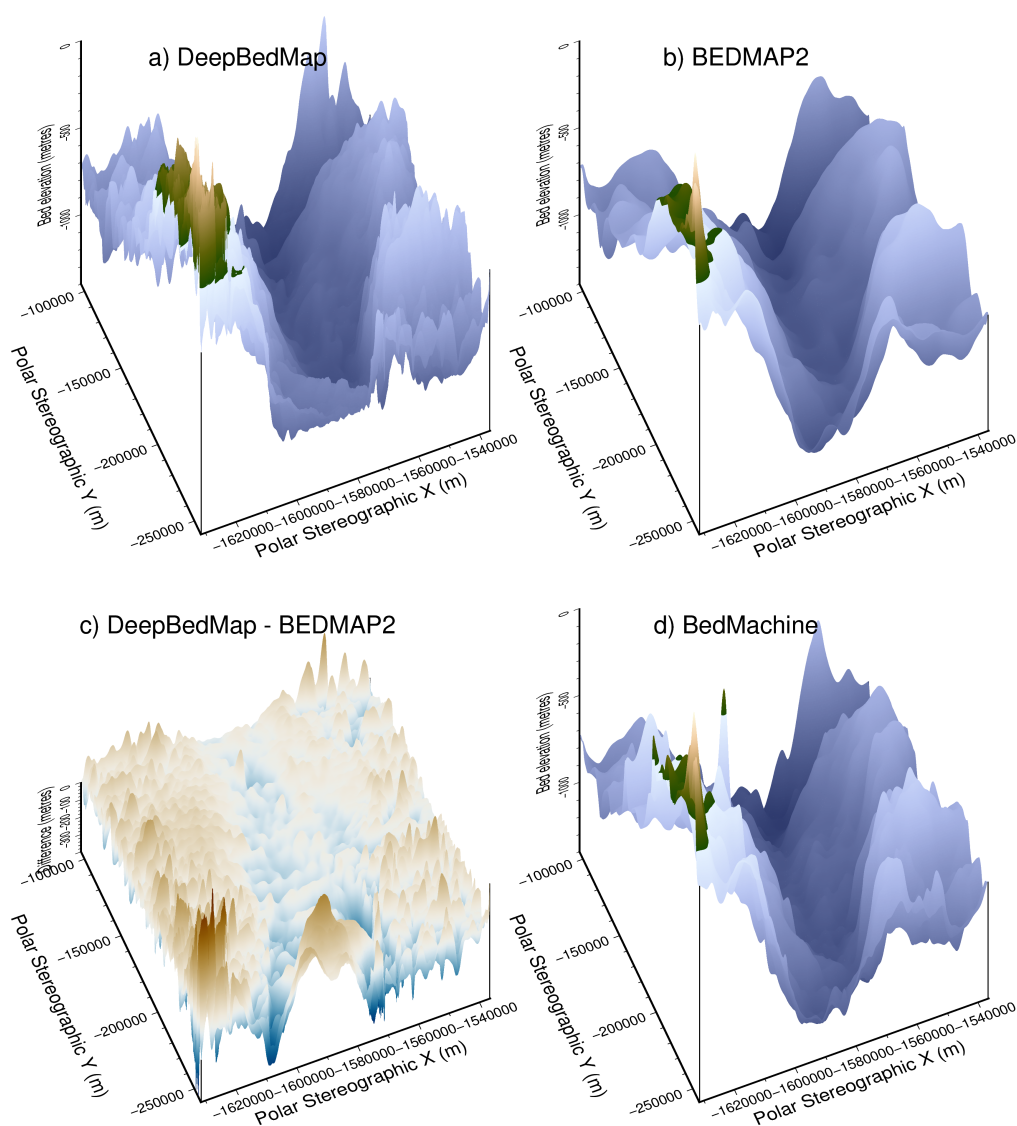
Figure 3. Comparison of interpolated bed elevation grid products over Pine Island Glacier (see extent in Figure 2). **a** DeepBedMap (ours) at 250 m resolution. **b** BEDMAP2 (Fretwell et al., 2013), originally 1000 m, bicubic interpolated to 250 m. **c** Elevation Difference between DeepBedMap and BEDMAP2. **d** BedMachine Antarctica (Morlighem, 2019), originally 500 m, bicubic interpolated to 250 m.
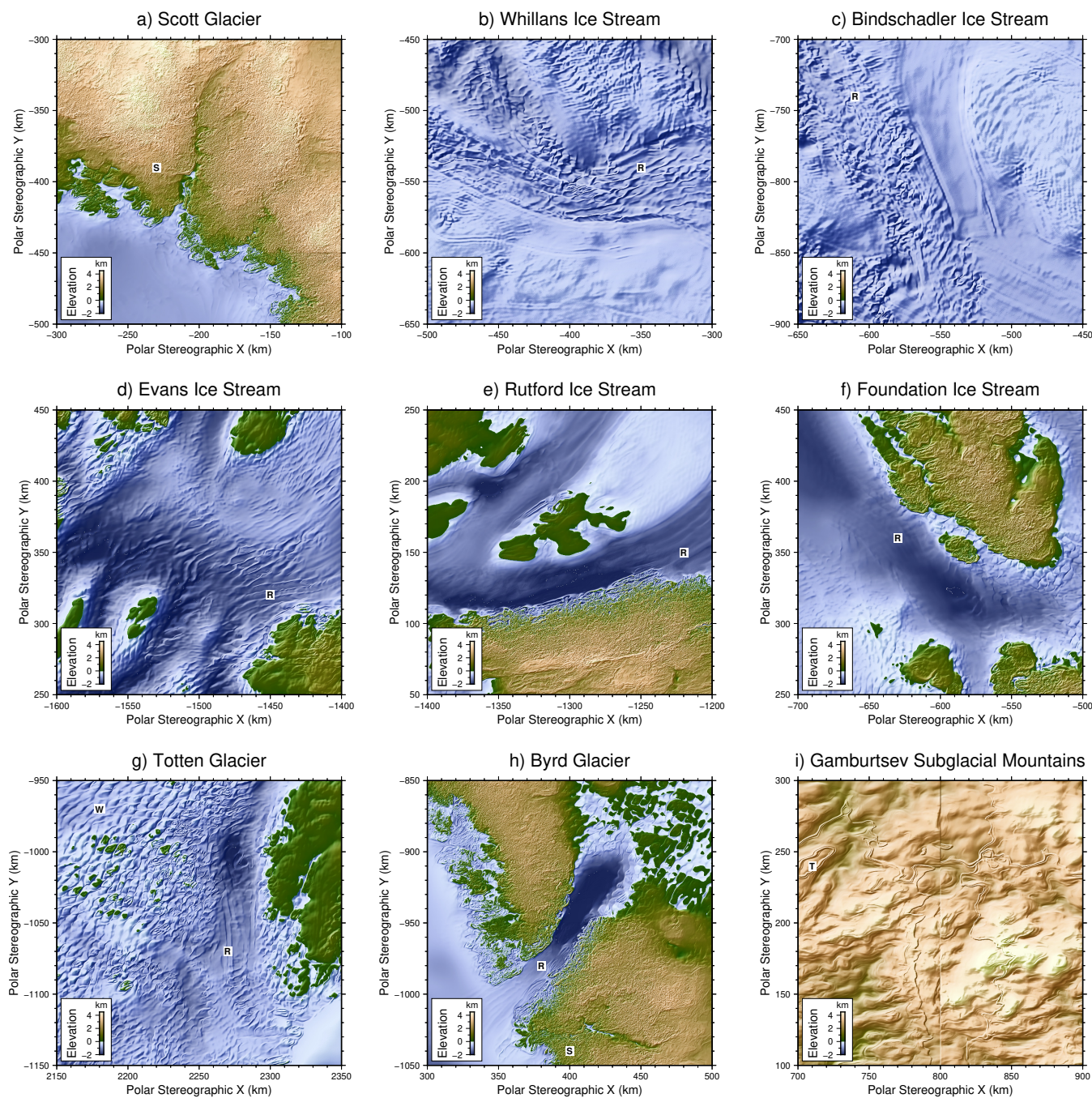
Figure 4. Closeup views of DeepBedMap_DEM around Antarctica. Top row shows Siple Coast locations. Middle row shows Weddell Sea region locations. Bottom row shows East Antarctica locations. Features of interest are annotated as black text against a white background: Ridges **R**, Speckle patterns **S**, Terraces **T**, Wave patterns **W**.

4.2 Surface Roughness

We compare the roughness of DeepBedMap_DEM versus BedMachine Antarctica with groundtruth grids from processed Operation IceBridge data (Shi et al., 2010) using standard deviation as a simple measure of roughness (Rippin et al., 2014). We calculate the surface roughness for a single 250 m pixel from the standard deviation of elevation values over a square 1250x1250 m area (i.e. 5x5 pixels) surrounding the central pixel. Focusing on Thwaites Glacier, the spatial 2D view of the DeepBedMap_DEM (Figure 5a) shows a range of typical topographic features such as hills and canyons. The calculated 2D roughness for both DeepBedMap_DEM (Figure 5b) and the Groundtruth (Figure 5c) lie in a similar range from 0 m to 400 m whereas the roughness of BedMachine Antarctica (Figure 5d) is mostly in the 0 m to 200 m range (hence the different colour scale). Also, the roughness pattern for both DeepBedMap_DEM and the Groundtruth has a more distributed cluster pattern made up of little pockets (especially towards the coastal region on the left, see Figure 5b and 5c), whereas the BedMachine Antarctica roughness pattern shows larger cluster pockets in isolated regions (see Figure 5d).

Taking a 1D transect over the 250 m resolution DeepBedMap_DEM, BedMachine Antarctica and groundtruth grids, we illustrate the differences in bed topography and roughness from the coast towards the inland area of Thwaites Glacier with a flight trace from Operation IceBridge (see Figure 6). For better comparison, we have calculated the Operation IceBridge groundtruth bed elevation and roughness values from a resampled 250 m grid instead of using its native along-track resolution. All three elevation profiles are shown to follow the same general trend from the relatively rough coastal region (Figure 6a from -1550 to -1500 km on x-scale), along the retrograde slope (Figure 6a from -1500 to -1450 km on x-scale), and into the interior region. DeepBedMap_DEM features a relatively noisy elevation profile with multiple fine-scale (<10 km) bumps and throughs similar to the groundtruth, while BedMachine Antarctica shows a smoother profile that is almost a moving average of the groundtruth elevation (Figure 6a). Looking at the roughness statistic (Figure 6b), both the DeepBedMap_DEM and Operation IceBridge groundtruth grids have a mean standard deviation of about 40 m whereas BedMachine Antarctica has a mean of about 10 m and rarely exceeds a standard deviation value of 20 m along the transect.

5 Discussion

5.1 Interpretation

In Section 4.1, we show that the DeepBedMap model has produced a high resolution (250 m) result (see Figure 3) that can capture a detailed and realistic picture of the underlying bed topography. The fine scale bumps and troughs are the result of the DeepBedMap Generator model learning to produce features that are similar to those found in the high resolution groundtruth datasets it was trained on. However, there are also artifacts produced by the model. For example, the winding terrace (**T**, Figure 4) features are hard to explain, and though they resemble eskers (Drews et al., 2017), their placement along the sides of hills does not support this view. Similarly, we are not sure why speckle (**S**, Figure 4) texture patterns are found over steep mountains, but the lack of high resolution training datasets likely leads the model to perform worse over these high gradient areas.
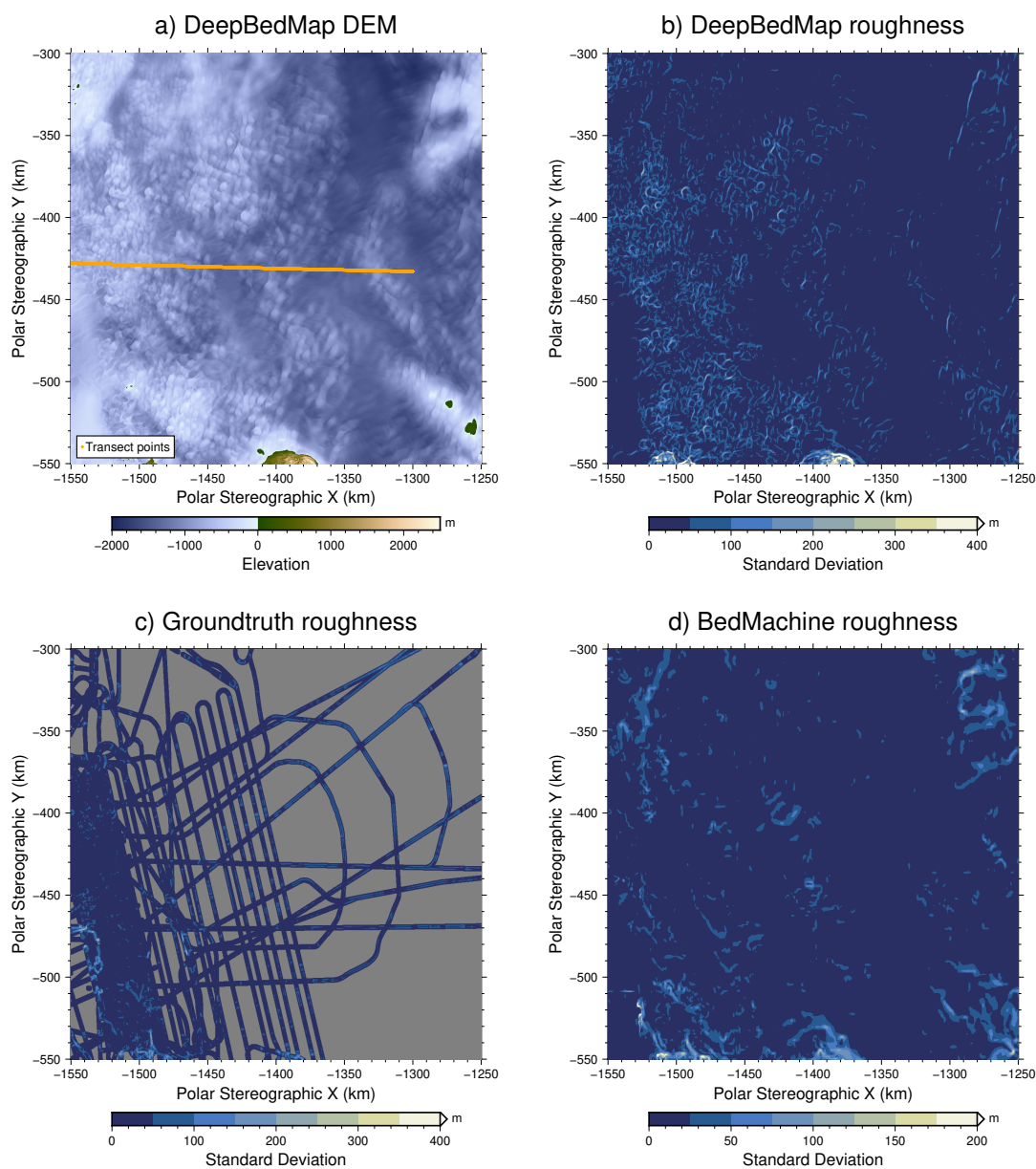
Figure 5. Spatial 2D view of grids over Thwaites Glacier, West Antarctica. Plotted on an Antarctic Stereographic Projection (EPSG:3031) with elevation and standard deviation values in metres referenced to the WGS84 datum. **a** DeepBedMap Digital Elevation Model. **b** 2D roughness from the DeepBedMap_DEM grid. **c** 2D roughness from interpolated Operation IceBridge grid. **d** 2D roughness from bicubic interpolated BedMachine Antarctica grid. Orange points in **a** correspond to transect sampling locations used in Figure 6. Note that color scale of **b** and **c** is two times that of **d**.
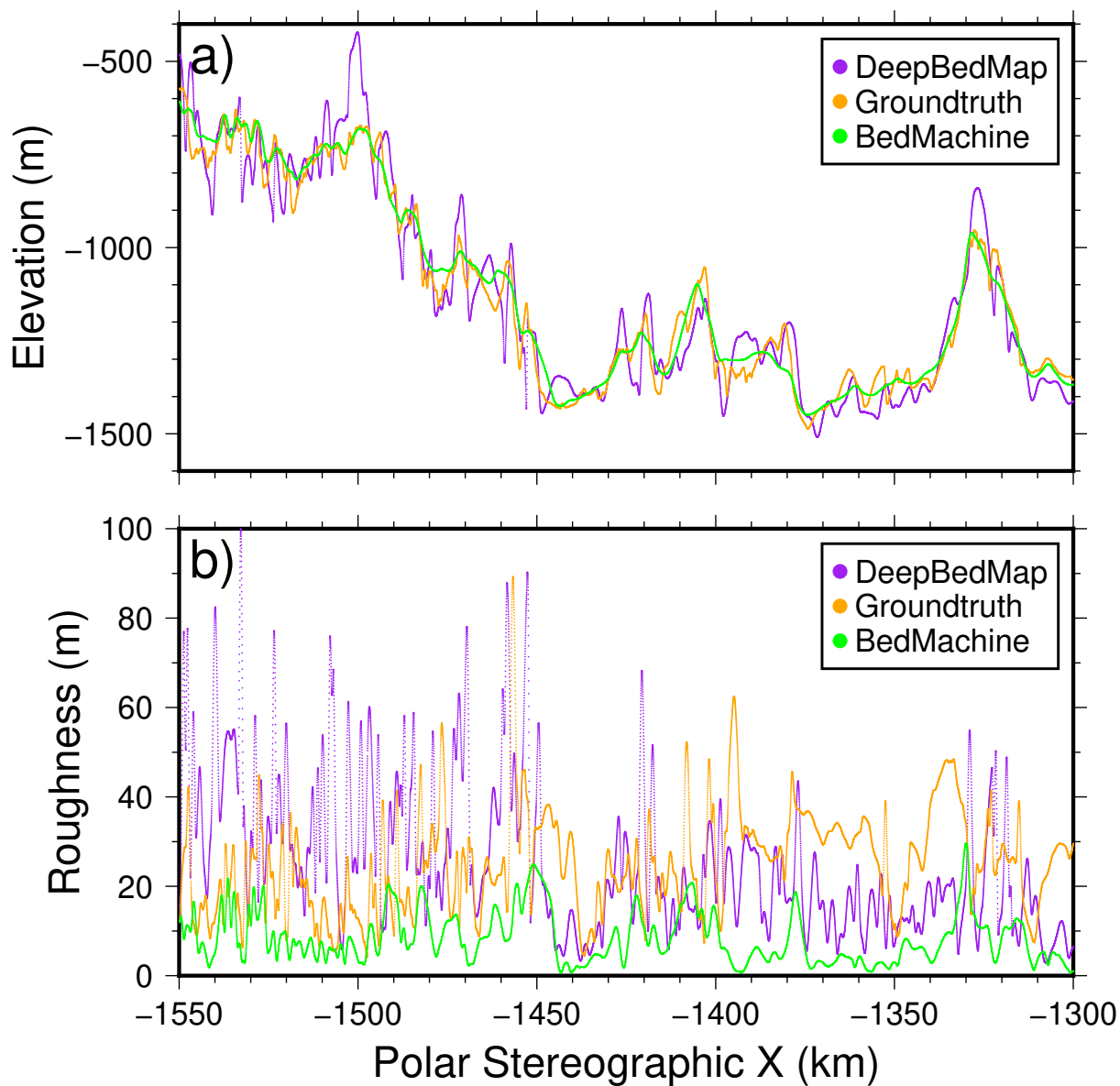
Figure 6. Comparing bed elevation **a** and surface roughness **b** (standard deviation of elevation values) of each interpolated grid product (250 m resolution) over a transect (see Figure 5 for location of transect line). Purple values are from the super resolution DeepBedMap_DEM; Orange values are from tension spline interpolated Operation IceBridge groundtruth points; Green values are from bicubic interpolated BedMachine Antarctica.

Another issue is that DeepBedMap will often pick up details from the high resolution ice surface elevation model (Howat et al., 2019) input dataset, which may not be representative of the true bed topography. For example, the ridges (**R**, Figure 4) found along fast flowing ice streams and glaciers are likely to be the imprints of crevasses or flowstripes (Glasser and Gudmundsson, 2012) observable from the surface. An alternative explanation is that the ridges, especially the honeycomb-

255 shaped ones, are rhombohedral moraine deposits formed by soft sediment squeezed up into basal crevasses that are sometimes found at stagnant surging glaciers (Dowdeswell et al., 2016a, b; Solheim and Louise Pfirman, 1985). We favour the first intepretation as the positions of these bed features coincide with the surface features, and also because these ridges are more likely to be eroded away in these fast flowing ice stream areas.

The hummocky wave-like (**W**) patterns we observe over the relatively flat and slower flowing areas are likely to result from

260 surface megadune structures (Scambos, 2014). Alternatively, they may be ribbed or rogen morraine features that are formed in an orientation transverse to the ice flow direction (Hättestrand, 1997; Hättestrand and Kleman, 1999). While any one of these two explanations may be valid in different regions of Antarctica, we lean towards the conservative interpretation that these features are the result of the DeepBedMap model overfitting to the ice surface elevation data.

In Section 4.2, we quantify that a well trained DeepBedMap neural network model can produce high roughness values more

265 comparable to the groundtruth than BedMachine Antarctica. While the mass conservation technique used by BedMachine Antarctica (Morlighem et al., 2019) improves upon ordinary interpolation techniques such as bicubic interpolation and kriging, their results are still inherently smooth by nature. The groundtruth grids show that rough areas do exist on a fine scale, and so the high resolution models we produce should reflect that.

DeepBedMap_DEM manages to capture much of the rough topography found in the Operation IceBridge groundtruth data,

270 especially near the coast (see Figure 6a, from -1550 to -1500 km on x-scale) where the terrain tends to be rougher. Along the retrograde slope (see Figure 6a, from -1500 to -1450 km on x-scale), several of the fine-scale (<10 km) bumps and troughs in DeepBedMap_DEM can be seen to correlate well in position with the groundtruth. In contrast, the cubic interpolated Bed-Machine Antarctica product lacks such fine-scale (<10 km) bumps and troughs, appearing as a relatively smooth terrain over much of the transect. Previous studies that estimated basal shear stress over Thwaites Glacier have found a band of strong

275 bed extending about 80-100 km from the grounding line, with pockets of weak bed interspersed between bands of strong bed further upstream (Joughin et al., 2009; Sergienko and Hindmarsh, 2013), a pattern that is broadly consistent with the DeepBedMap_DEM roughness results (see Figure 5b). In general, DeepBedMap_DEM produces a topography that is much more rougher, with standard deviation values more in line with those observed in the groundtruth (see Figure 6b). The rough-ness values for BedMachine Antarctica are consistently lower throughout the transect, a consequence of the mass conservation

280 technique using regularization parameters that yields smooth results. Recent studies have stressed the importance of form drag (basal drag due to bed topography) over skin drag (or basal friction) on the basal traction of Pine Island Glacier (Bingham et al., 2017; Kyrke-Smith et al., 2018), and the DeepBedMap super-resolution work here shows strong potential in meeting that demand as a realistic high resolution bed topography dataset for ice sheet modelling studies.

5.2 Limitations

285 The DeepBedMap model is trained only on a small fraction of the area of Antarctica, simply because the convolutional neural network cannot be trained on sparse survey point measurements. The topography generated by the model is quite sensitive to the accuracy of its data inputs (see Table 1 and 2), and though this is a problem faced by many other inverse methods, neural network models like ours can be particularly biased towards the training dataset.

An inherent assumption in this methodology is that the training data sets have sampled the variable bed lithology of Antarc-
290 tica (Cox et al., 2018) sufficiently. This is unlikely to be true, introducing uncertainty in the result as different lithologies may cause the same macro-scale bed landscapes to result in a range of surface features. In particular, the experimental model's topography is likely skewed towards the distribution of the training regions that tend to reside in coastal regions, especially over ice streams in West Antarctica (see Figure 2). Besides collecting more radio-echo sounding datasets to sample these regions more densely, swath reprocessing of old datasets that have that capability (Holschuh et al., 2019) may be another useful
295 addition to the training set.

5.3 Future directions

While care has been taking to source the best possible datasets (see Table 1 and 2), we note that there is still room to improve the DeepBedMap_DEM's results. Some of the conditional datasets we use such as REMA (Howat et al., 2019) and MEaSUREs Ice Velocity (Mouginot et al., 2019b) contain data gaps which introduce artifacts in the DeepBedMap_DEM, and those holes
300 need to be patched up for proper continent-wide prediction. As the DeepBedMap model relies on data from multiple sources which are collected over different epochs, it has no proper sense of time. Ice elevation change captured using satellite altimeters (e.g. from ICESat-2 (Markus et al., 2017)) could be added as an additional input to better account for temporal factors. It is possible to apply the super resolution DeepBedMap technique on bed elevation inputs newer than BEDMAP2 (Fretwell et al., 2013), such as the 1000 m resolution DEM over the Weddell Sea (Jeofry et al., 2017) or the 500 m resolution Bedmachine
305 Antarctica dataset (Morlighem, 2019).

Our DeepBedMap model is modular by design, and the different modules (see Figure 1) can be improved on and adapted for future use cases. The architecture of the input module can be modified to handle new datasets such as the ones suggested above, or redesigned to extract a greater amount of information for better performance. Similarly, the core and upsampling modules which are based on ESRGAN (Wang et al., 2018) can be replaced with newer, better architectures as the need arises.
310 The redesigned neural network model can be retrained from scratch or fine-tuned using the trained weights from DeepBedMap to further improve the predictive performance. Taken together, these advances will lead to an even more accurate and higher resolution bed elevation model.

6 Conclusions

The DeepBedMap convolutional neural network method presents a data-driven approach to better resolve the bed topography
315 of Antarctica using existing data. It is an improvement beyond simple interpolation techniques, generating realistic high spatial
resolution (250 m) topography that preserves detail in bed roughness and is adaptable for catchment to continent-scale studies
on ice sheets. Unlike other inverse methods that rely on some explicit parameterization of ice-flow physics, the model uses
deep learning to find suitable neural network parameters via an iterative error minimization approach. This makes the resulting
model particularly sensitive to the training data set, emphasizing the value of densely spaced bed elevation datasets and the
320 need for such sampling over a more diverse range of Antarctic substrate types. The use of Graphical Processing Units (GPUs)
for training and inference allows the neural network method to scale easily, and the addition of more training datasets will
allow it to perform better.

The work here is not intended to discourage the usage of other inverse modelling techniques, but to introduce an independent
methodology, with an outlook towards combining the strengths of the two. Once properly trained, the DeepBedMap model runs
325 quickly and produces realistic rough topography, which when merged with more physically based mass conservation inverse
approaches (e.g. Morlighem et al., 2019) will likely result in more efficient ways of generating accurate bed elevation maps
of Antarctica. One side product resulting from this work is a test-driven development framework that can be used to measure
and compare the performance of upcoming bed terrain models. The radioglaciology community has already begun to compile
a new comprehensive bed elevation/ice thickness dataset for Antarctica, and there has been discussions to combine various
330 terrain interpolation techniques in an ensemble to collaboratively create the new BEDMAP3.

Code availability. Python code for data preparation, neural network model training and visualization of model outputs are freely available at
https://github.com/weiji14/deepbedmap. Neural network model training experiment runs are also recorded at https://www.comet.ml/weiji14/deepbedmap.

Data availability. DeepBedMap_DEM available through the Open Science Framework platform at https://doi.org/10.17605/OSF.IO/96APW.
Pine Island Glacier dataset (Bingham et al., 2017) available on request from Robert Bingham. Carlson Inlet dataset (King, 2011) avail-
335 able on request from Edward King. Bed elevation datasets from Wilkes Subglacial Basin (Ferraccioli et al., 2018) and Rutford Ice Stream
(King et al., 2016) available from British Antarctic Survey's Polar Data Centre (https://ramadda.data.bas.ac.uk). Other Antarctic bed el-
evation datasets available from Center for Remote Sensing of Ice Sheets (https://data.cresis.ku.edu/data/rds) or from National Snow and
Ice Data Center (https://nsidc.org/data/IRMCR2/versions/1). BEDMAP2 (Fretwell et al., 2013) and REMA (Howat et al., 2018) avail-
able from Polar Geospatial Center (http://data.pgc.umn.edu). MEaSUREs ice velocity data (Mouginot et al., 2019b) available from NSIDC
340 (https://nsidc.org/data/nsidc-0754/versions/1). Antarctic Snow Accummulation data (Arthern et al., 2006) available from British Antarctic
Survey (https://secure.antarctica.ac.uk/data/bedmap2/resources/Arthern_accumulation).

Appendix A: Details of loss function components

The loss function, or cost function, is a mathematical function that maps a set of input variables to an output loss value. The loss value can be thought of as a weighted sum of several error metrics between the neural network's prediction and the expected output or groundtruth. It is this loss value which we want to minimize so as to train the neural network model to perform better, and we do this by iteratively optimizing the parameters in the loss function. Following this are the details of the various loss functions that make up the total loss function of the DeepBedMap Generative Adversarial Network model.

A1   Content Loss

To bring the pixel values of the generated images closer to that of the groundtruth, we first define the Content Loss function L_1. Following ESRGAN (Wang et al., 2018), we have:

$$L_1 = \frac{1}{n} \sum_{i=1}^{n} ||\hat{y}_i - y_i||_1 \tag{A1}$$

where we take the mean absolute error between the Generator Network's predicted value $\hat{y}_i$ and the groundtruth value y_i, respectively over every pixel i.

A2   Adversarial Loss

Next, we define an Adversarial Loss to encourage the production of high resolution images $\hat{y}$ closer to the manifold of natural looking digital elevation model images. To do so, we introduce the standard discriminator in the form of $D(y) = \sigma(C(y))$ where σ is the sigmoid activation function and $C(y)$ is the raw, non-transformed output from a discriminator neural network acting on high resolution image y. The ESRGAN model (Wang et al., 2018) however, employs an improved Relativistic-average Discriminator (Jolicoeur-Martineau, 2018) denoted by D_{Ra}. It is defined as $D_{Ra}(y, \hat{y}) = \sigma(C(y) - \mathbb{E}_{\hat{y}}[C(\hat{y})])$, where $\mathbb{E}_{\hat{y}}[\cdot]$ is the arithmetic mean operation carried out over every generated image $\hat{y}$ in a mini-batch. We use a binary cross entropy loss as the discriminator's loss function defined as follows:

$$L_D^{Ra} = -\mathbb{E}_y[\ln(D(y, \hat{y}))] - \mathbb{E}_{\hat{y}}[\ln(1 - D(\hat{y}, y))] \tag{A2}$$

The generator network's adversarial loss is in a symmetrical form:

$$L_G^{Ra} = -\mathbb{E}_y[\ln(1 - D(y, \hat{y}))] - \mathbb{E}_{\hat{y}}[\ln(D(\hat{y}, y))] \tag{A3}$$

A3   Topographic Loss

We further define a Topographic Loss so that the elevation values in the super resolved image make topographic sense with respect to the original low resolution image. Specifically, we want the mean value of each 4x4 grid on the predicted super

resolution (DeepBedMap) image to closely match its spatially corresponding 1x1 pixel on the low resolution (BEDMAP2) image.

370 First, we apply a 4x4 Mean Pooling operation on the Generator Network's predicted super resolution image:

$$\bar{\hat{y}}_j = \frac{1}{n}\sum_{i=1}^{n}\hat{y}_i \tag{A4}$$

where $\bar{\hat{y}}_j$ is the mean of all predicted values $\hat{y}_i$ across the 16 super-resolved pixels i within a 4x4 grid corresponding to the spatial location of one low resolution pixel at position j. Following this, we can compute the Topographic Loss as follows:

$$L_T = \frac{1}{m}\sum_{i=1}^{m}||\bar{\hat{y}}_j - x_j||_1 \tag{A5}$$

375 where we take the mean absolute error between the mean of the 4x4 super-resolved pixels calculated in Equation (A4) $\bar{\hat{y}}_j$ and that of the spatially corresponding low resolution pixel x_j, respectively over every low resolution pixel j.

A4 Structural Loss

Lastly, we define a Structural Loss that takes into account luminance, contrast and structural information between the predicted and groundtruth images. This is based on the Structural Similarity Index (SSIM, Wang et al., 2004) and is calculated over a
380 single window patch as so:

$$SSIM(\hat{y}, y) = \frac{(2\mu_{\hat{y}}\mu_y + c_1)(2\sigma_{\hat{y}y} + c_2)}{(\mu_{\hat{y}}^2 + \mu_y^2 + c_1)(\sigma_{\hat{y}}^2 + \sigma_y^2 + c_2)} \tag{A6}$$

where $\mu_{\hat{y}}$ and μ_y are the arithmetic mean of predicted image $\hat{y}$ and groundtruth image y respectively over a single window that we set to 9x9 pixels, $\sigma_{\hat{y}y}$ is the covariance of $\hat{y}$ and y, $\sigma_{\hat{y}}^2$ and σ_y^2 are the variance of $\hat{y}$ and y respectively, and c_1 and c_2 are two variables set to 0.01^2 and 0.03^2 to stabilize division with a weak denominator. Thus, we can formulate the Structural Loss
385 as follows:

$$L_S = 1 - \frac{1}{p}\sum_{i=1}^{p}SSIM(\hat{y}, y)_p \tag{A7}$$

where we do 1 minus the mean of all structural similarity values $SSIM(\hat{y}, y)$ calculated over every patch p obtained via a sliding window over the predicted image $\hat{y}$ and groundtruth image y.

A5 Total Loss Function

390 Finally, we compile the loss functions for the discriminator and generator networks as follows:

$$L_D = L_D^{Ra} \tag{A8}$$

$$L_G = \eta L_1 + \lambda L_G^{Ra} + \theta L_T + \zeta L_S \tag{A9}$$

where η, λ, θ, and ζ are the scaled weights for the content L_1, adversarial L_D, topographic L_T and structural losses L_S respectively (see Table B1 for values used). The loss functions L_D and L_G are minimized in an alternate 1:1 manner so as to solve the entire Generative Adversarial Network's objective function defined in Equation (4).

Appendix B: Neural Network Training Details

The neural networks were developed using Chainer v7.0.0b2 (Tokui et al., 2019), and trained using full precision (floating point 32) arithmetic. Experiments were carried out on 4 Graphical Processing Units (GPUs), specifically 2 Tesla P100 GPUs and 2 Tesla V100 GPUs. On the Tesla V100 GPU setup, one training run with about 150 epochs takes about 30 minutes. This is using a batch size of 128 on a total of 3826 training image tiles, with 202 tiles reserved for validation, i.e. a 95/5 training/validation split. We next describe the method used to evaluate each DeepBedMap candidate model, as well as the high-level way in which we semi-automatically arrived at a good model via semi-automatic hyperparameter tuning.

Table B1. Optimized Hyperparameter Settings.

Hyperparameter	Setting	Tuning Range
Learning rate (for both Generator and Discriminator)	1.7e-4	2e-4 to 1e-4
Number of Residual-in-Residual Blocks	12	8 to 14
Mini-batch size	128	64 or 128
Number of epochs	140	90 to 150
Residual scaling	0.2	0.1 to 0.5
Content Loss Weighting η	1e-2	Fixed
Adversarial Loss Weighting λ	2e-2	Fixed
Topographic Loss Weighting θ	2e-3	Fixed
Structural Loss Weighting ζ	5.25	Fixed
He Normal Initialization Scaling	0.1	Fixed
Adam optimizer epsilon	0.1	Fixed
Adam optimizer beta1	0.9	Fixed
Adam optimizer beta2	0.99	Fixed

To check for overfitting, we evaluate the Generative Adversarial Network model on the validation dataset after each epoch using two performance metrics - a peak signal-to-noise ratio (PSNR) metric for the Generator, and an accuracy metric for the Discriminator. Training stops when these validation performance metrics show little improvement, roughly at 120 epochs.

Next, we conduct a full evaluation on an independent test dataset, comparing the model's predicted grid output against actual groundtruth xyz points. Using the 'grdtrack' function in Generic Mapping Tools v6.0 (Wessel et al., 2019), we obtain the grid elevation at each groundtruth point and use it to calculate the elevation error on a point-to-point basis. All of these elevation errors are then used to compute a Root Mean Squared Error (RMSE) statistic over this independent test site. This RMSE value is used to judge the model's performance in relation to baseline bicubic interpolation, and also the metric minimized by a hyperparameter optimization algorithm which we will describe next.

Neural networks contain a lot of hyperparameter settings that need to be decided upon, and Generative Adversarial Networks are particularly sensitive to different hyperparameter settings. To stabilize model training and obtain better performance, we tune the hyperparameters (see Table B1) using a Bayesian approach. Specifically, we employ the Tree-structured Parzen Estimator (Bergstra et al., 2011) from the Optuna v0.14.0 (Akiba et al., 2019) library with default settings as per the Hyperopt library (Bergstra et al., 2015). Given that we have 4 GPUs, we choose to parallelize the hyperparameter tuning experiments asynchronously between all four devices. The estimator first conducts 20 random experimental trials to scan the hyperparameter space, gradually narrowing down to a few candidate hyperparameters in subsequent experiments. We set each GPU to run a target of 30 experimental trials (i.e. a total of 120), though unpromising trials that have exploding/vanishing gradients are pruned prematurely to save on time and computational resources. The top models from these experiments undergo further visual evaluation, and we continue to conduct further experiments until a suitable candidate model is found.

Author contributions. W. J. L. - conceptualisation, data curation, formal analysis, methodology, software, visualization, writing – original draft, writing – review & editing. H. J. H. - conceptualisation, funding acquisition, supervision, writing – review & editing.

Competing interests. The authors declare that they have no conflict of interest.

Acknowledgements. We are grateful to Robert Bingham and Edward King for the Pine Island Glacier and Carlson Inlet data, and to all the other researchers in the British Antarctic Survey and Operation IceBridge team for providing free access to the high resolution bed elevation datasets around Antarctica. A special thanks to Ruzica Dadic for her help in reviewing draft versions of this paper. This research was funded by the Royal Society of New Zealand's Rutherford Discovery Fellowship (Contract: RDF-VUW1602), with additional support from the Erasmus+ programme and International Glaciological Society early career travel award for presenting earlier versions of this work at the 2019 EGU General Assembly and IGS Symposium on Five Decades of Radioglaciology.

References

Akiba, T., Sano, S., Yanase, T., Ohta, T., and Koyama, M.: Optuna: A Next-Generation Hyperparameter Optimization Framework, in: Proceedings of the 25th ACM SIGKDD International Conference on Knowledge Discovery & Data Mining - KDD '19, pp. 2623–2631, ACM Press, Anchorage, AK, USA, https://doi.org/10.1145/3292500.3330701, 2019.

435 Arthern, R. J., Winebrenner, D. P., and Vaughan, D. G.: Antarctic Snow Accumulation Mapped Using Polarization of 4.3-Cm Wavelength Microwave Emission, Journal of Geophysical Research, 111, https://doi.org/10.1029/2004JD005667, 2006.

Bergstra, J., Bardenet, R., Bengio, Y., and Kégl, B.: Algorithms for Hyper-Parameter Optimization, in: Proceedings of the 24th International Conference on Neural Information Processing Systems, NIPS'11, pp. 2546–2554, Curran Associates Inc., Granada, Spain, 2011.

Bergstra, J., Komer, B., Eliasmith, C., Yamins, D., and Cox, D. D.: Hyperopt: A Python Library for Model Selection and Hyperparameter
440 Optimization, Computational Science & Discovery, 8, 014 008, https://doi.org/10.1088/1749-4699/8/1/014008, 2015.

Bingham, R. G., Vaughan, D. G., King, E. C., Davies, D., Cornford, S. L., Smith, A. M., Arthern, R. J., Brisbourne, A. M., De Rydt, J., Graham, A. G. C., Spagnolo, M., Marsh, O. J., and Shean, D. E.: Diverse Landscapes beneath Pine Island Glacier Influence Ice Flow, Nature Communications, 8, https://doi.org/10.1038/s41467-017-01597-y, 2017.

Blau, Y., Mechrez, R., Timofte, R., Michaeli, T., and Zelnik-Manor, L.: 2018 PIRM Challenge on Perceptual Image Super-Resolution, 2018.

445 Chen, Z., Wang, X., Xu, Z., and Hou, W.: Convolutional Neural Network Based Dem Super Resolution, ISPRS - International Archives of the Photogrammetry, Remote Sensing and Spatial Information Sciences, XLI-B3, 247–250, https://doi.org/10.5194/isprsarchives-XLI-B3-247-2016, 2016.

Clarke, G. K. C., Berthier, E., Schoof, C. G., and Jarosch, A. H.: Neural Networks Applied to Estimating Subglacial Topography and Glacier Volume, Journal of Climate, 22, 2146–2160, https://doi.org/10.1175/2008JCLI2572.1, 2009.

450 Cornford, S. L., Martin, D. F., Lee, V., Payne, A. J., and Ng, E. G.: Adaptive Mesh Refinement versus Subgrid Friction Interpolation in Simulations of Antarctic Ice Dynamics, Annals of Glaciology, 57, 1–9, https://doi.org/10.1017/aog.2016.13, 2016.

Cox, S. C., Smith-Lyttle, B., Siddoway, C., Capponi, G., Elvevold, S., Burton-Johnson, A., Halpin, J., Morin, P., Elliot, D., and Geomap Action Group: The GeoMAP Dataset of Antarctic Rock Exposures, in: POLAR2018, p. 2428, Davos, Switzerland, 2018.

Dai, J., Qi, H., Xiong, Y., Li, Y., Zhang, G., Hu, H., and Wei, Y.: Deformable Convolutional Networks, arXiv:1703.06211 [cs], 2017.

455 Dong, C., Loy, C. C., He, K., and Tang, X.: Image Super-Resolution Using Deep Convolutional Networks, arXiv:1501.00092 [cs], 2014.

Dowdeswell, J. A., Canals, M., Jakobsson, M., Todd, B. J., Dowdeswell, E. K., and Hogan, K. A.: The Variety and Distribution of Submarine Glacial Landforms and Implications for Ice-Sheet Reconstruction, Geological Society, London, Memoirs, 46, 519–552, https://doi.org/10.1144/M46.183, 2016a.

Dowdeswell, J. A., Solheim, A., and Ottesen, D.: Rhombohedral Crevasse-Fill Ridges at the Marine Margin of a Surging Svalbard Ice Cap,
460 Geological Society, London, Memoirs, 46, 73–74, https://doi.org/10.1144/M46.62, 2016b.

Drews, R., Pattyn, F., Hewitt, I. J., Ng, F. S. L., Berger, S., Matsuoka, K., Helm, V., Bergeot, N., Favier, L., and Neckel, N.: Actively Evolving Subglacial Conduits and Eskers Initiate Ice Shelf Channels at an Antarctic Grounding Line, Nature Communications, 8, https://doi.org/10.1038/ncomms15228, 2017.

Dumoulin, V., Perez, E., Schucher, N., Strub, F., Vries, H., Courville, A., and Bengio, Y.: Feature-Wise Transformations, Distill, 3,
465 https://doi.org/10.23915/distill.00011, 2018.

Durand, G., Gagliardini, O., Favier, L., Zwinger, T., and le Meur, E.: Impact of Bedrock Description on Modeling Ice Sheet Dynamics: BEDROCK DESCRIPTION TO MODEL ICE SHEET, Geophysical Research Letters, 38, n/a–n/a, https://doi.org/10.1029/2011GL048892, 2011.

Falcini, F. A., Rippin, D. M., Krabbendam, M., and Selby, K. A.: Quantifying Bed Roughness beneath Contemporary and Palaeo-Ice Streams, Journal of Glaciology, 64, 822–834, https://doi.org/10.1017/jog.2018.71, 2018.

Farinotti, D., Huss, M., Bauder, A., Funk, M., and Truffer, M.: A Method to Estimate the Ice Volume and Ice-Thickness Distribution of Alpine Glaciers, Journal of Glaciology, 55, 422–430, https://doi.org/10.3189/002214309788816759, 2009.

Farinotti, D., Brinkerhoff, D. J., Clarke, G. K. C., Fürst, J. J., Frey, H., Gantayat, P., Gillet-Chaulet, F., Girard, C., Huss, M., Leclercq, P. W., Linsbauer, A., Machguth, H., Martin, C., Maussion, F., Morlighem, M., Mosbeux, C., Pandit, A., Portmann, A., Rabatel, A., Ramsankaran, R., Reerink, T. J., Sanchez, O., Stentoft, P. A., Singh Kumari, S., van Pelt, W. J. J., Anderson, B., Benham, T., Binder, D., Dowdeswell, J. A., Fischer, A., Helfricht, K., Kutuzov, S., Lavrentiev, I., McNabb, R., Gudmundsson, G. H., Li, H., and Andreassen, L. M.: How Accurate Are Estimates of Glacier Ice Thickness? Results from ITMIX, the Ice Thickness Models Intercomparison eXperiment, The Cryosphere, 11, 949–970, https://doi.org/10.5194/tc-11-949-2017, 2017.

Farinotti, D., Huss, M., Fürst, J. J., Landmann, J., Machguth, H., Maussion, F., and Pandit, A.: A Consensus Estimate for the Ice Thickness Distribution of All Glaciers on Earth, Nature Geoscience, 12, 168–173, https://doi.org/10.1038/s41561-019-0300-3, 2019.

Ferraccioli, F., Corr, H., Jordan, T., Robinson, C., Armadillo, E., Armadillo, E., and Armadillo, G.: Airborne Radar Bed Elevation Picks across the Wilkes Subglacial Basin, 2005-2006, https://doi.org/10.5285/59e5a6f5-e67d-4a05-99af-30f656569401, 2018.

Fretwell, P., Pritchard, H. D., Vaughan, D. G., Bamber, J. L., Barrand, N. E., Bell, R., Bianchi, C., Bingham, R. G., Blankenship, D. D., Casassa, G., Catania, G., Callens, D., Conway, H., Cook, A. J., Corr, H. F. J., Damaske, D., Damm, V., Ferraccioli, F., Forsberg, R., Fujita, S., Gim, Y., Gogineni, P., Griggs, J. A., Hindmarsh, R. C. A., Holmlund, P., Holt, J. W., Jacobel, R. W., Jenkins, A., Jokat, W., Jordan, T., King, E. C., Kohler, J., Krabill, W., Riger-Kusk, M., Langley, K. A., Leitchenkov, G., Leuschen, C., Luyendyk, B. P., Matsuoka, K., Mouginot, J., Nitsche, F. O., Nogi, Y., Nost, O. A., Popov, S. V., Rignot, E., Rippin, D. M., Rivera, A., Roberts, J., Ross, N., Siegert, M. J., Smith, A. M., Steinhage, D., Studinger, M., Sun, B., Tinto, B. K., Welch, B. C., Wilson, D., Young, D. A., Xiangbin, C., and Zirizzotti, A.: Bedmap2: Improved Ice Bed, Surface and Thickness Datasets for Antarctica, The Cryosphere, 7, 375–393, https://doi.org/10.5194/tc-7-375-2013, 2013.

Fukushima, K. and Miyake, S.: Neocognitron: A New Algorithm for Pattern Recognition Tolerant of Deformations and Shifts in Position, Pattern Recognition, 15, 455–469, https://doi.org/10.1016/0031-3203(82)90024-3, 1982.

Glasser, N. F. and Gudmundsson, G. H.: Longitudinal Surface Structures (Flowstripes) on Antarctic Glaciers, The Cryosphere, 6, 383–391, https://doi.org/10.5194/tc-6-383-2012, 2012.

Goodfellow, I. J., Pouget-Abadie, J., Mirza, M., Xu, B., Warde-Farley, D., Ozair, S., Courville, A., and Bengio, Y.: Generative Adversarial Networks, arXiv:1406.2661 [cs, stat], 2014.

Graham, F. S., Roberts, J. L., Galton-Fenzi, B. K., Young, D., Blankenship, D., and Siegert, M. J.: A High-Resolution Synthetic Bed Elevation Grid of the Antarctic Continent, Earth System Science Data, 9, 267–279, https://doi.org/10.5194/essd-9-267-2017, 2017.

Hättestrand, C.: Ribbed Moraines in Sweden — Distribution Pattern and Palaeoglaciological Implications, Sedimentary Geology, 111, 41–56, https://doi.org/10.1016/S0037-0738(97)00005-5, 1997.

Hättestrand, C. and Kleman, J.: Ribbed Moraine Formation, Quaternary Science Reviews, 18, 43–61, https://doi.org/10.1016/S0277-3791(97)00094-2, 1999.

He, K., Zhang, X., Ren, S., and Sun, J.: Deep Residual Learning for Image Recognition, arXiv:1512.03385 [cs], 2015.

He, K., Zhang, X., Ren, S., and Sun, J.: Identity Mappings in Deep Residual Networks, arXiv:1603.05027 [cs], 2016.

505 Holschuh, N., Christianson, K., and Paden, J.: Swath Topography, and the Future of Polar Bed Mapping, in: IGS Symposium on Five Decades of Radioglaciology, Stanford University, 2019.

Howat, I. M., Morin, Paul, Porter, Claire, and Noh, Myong-Jong: The Reference Elevation Model of Antarctica, https://doi.org/10.7910/DVN/SAIK8B, 2018.

Howat, I. M., Porter, C., Smith, B. E., Noh, M.-J., and Morin, P.: The Reference Elevation Model of Antarctica, The Cryosphere, 13, 665–674,
510 https://doi.org/10.5194/tc-13-665-2019, 2019.

Ioffe, S. and Szegedy, C.: Batch Normalization: Accelerating Deep Network Training by Reducing Internal Covariate Shift, arXiv:1502.03167 [cs], 2015.

Isola, P., Zhu, J.-Y., Zhou, T., and Efros, A. A.: Image-to-Image Translation with Conditional Adversarial Networks, arXiv:1611.07004 [cs], 2016.

515 Jeofry, H., Ross, N., Corr, H. F., Li, J., Gogineni, P., and Siegert, M. J.: 1-Km Bed Topography Digital Elevation Model (Dem) Of The Weddell Sea Sector, West Antarctica, https://doi.org/10.5281/zenodo.1035488, 2017.

Jolicoeur-Martineau, A.: The Relativistic Discriminator: A Key Element Missing from Standard GAN, arXiv:1807.00734 [cs, stat], 2018.

Jordan, T. A., Ferraccioli, F., Corr, H., Graham, A., Armadillo, E., and Bozzo, E.: Hypothesis for Mega-Outburst Flooding from a Palaeo-Subglacial Lake beneath the East Antarctic Ice Sheet: Antarctic Palaeo-Outburst Floods and Subglacial Lake, Terra Nova, 22, 283–289,
520 https://doi.org/10.1111/j.1365-3121.2010.00944.x, 2010.

Joughin, I., Tulaczyk, S., Bamber, J. L., Blankenship, D., Holt, J. W., Scambos, T., and Vaughan, D. G.: Basal Conditions for Pine Island and Thwaites Glaciers, West Antarctica, Determined Using Satellite and Airborne Data, Journal of Glaciology, 55, 245–257, https://doi.org/10.3189/002214309788608705, 2009.

King, E. C.: Ice Stream or Not? Radio-Echo Sounding of Carlson Inlet, West Antarctica, The Cryosphere, 5, 907–916,
525 https://doi.org/10.5194/tc-5-907-2011, 2011.

King, E. C., Pritchard, H. D., and Smith, A. M.: Subglacial Landforms beneath Rutford Ice Stream, Antarctica: Detailed Bed Topography from Ice-Penetrating Radar, Earth System Science Data, 8, 151–158, https://doi.org/10.5194/essd-8-151-2016, 2016.

Krizhevsky, A., Sutskever, I., and Hinton, G. E.: ImageNet Classification with Deep Convolutional Neural Networks, in: Advances in Neural Information Processing Systems 25, edited by Pereira, F., Burges, C. J. C., Bottou, L., and Weinberger, K. Q., pp. 1097–1105, Curran
530 Associates, Inc., 2012.

Kyrke-Smith, T. M., Gudmundsson, G. H., and Farrell, P. E.: Relevance of Detail in Basal Topography for Basal Slipperiness Inversions: A Case Study on Pine Island Glacier, Antarctica, Frontiers in Earth Science, 6, https://doi.org/10.3389/feart.2018.00033, 2018.

LeCun, Y., Boser, B., Denker, J. S., Henderson, D., Howard, R. E., Hubbard, W., and Jackel, L. D.: Backpropagation Applied to Handwritten Zip Code Recognition, Neural Computation, 1, 541–551, https://doi.org/10.1162/neco.1989.1.4.541, 1989.

535 Lecun, Y., Bottou, L., Bengio, Y., and Haffner, P.: Gradient-Based Learning Applied to Document Recognition, Proceedings of the IEEE, 86, 2278–2324, https://doi.org/10.1109/5.726791, 1998.

LeCun, Y., Bengio, Y., and Hinton, G.: Deep Learning, Nature, 521, 436–444, https://doi.org/10.1038/nature14539, 2015.

Ledig, C., Theis, L., Huszar, F., Caballero, J., Cunningham, A., Acosta, A., Aitken, A., Tejani, A., Totz, J., Wang, Z., and Shi, W.: Photo-Realistic Single Image Super-Resolution Using a Generative Adversarial Network, 2016.

540 Lim, B., Son, S., Kim, H., Nah, S., and Lee, K. M.: Enhanced Deep Residual Networks for Single Image Super-Resolution, arXiv:1707.02921 [cs], 2017.

Liu, X., Wang, Y., and Liu, Q.: PSGAN: A Generative Adversarial Network for Remote Sensing Image Pan-Sharpening, arXiv:1805.03371 [cs], 2018.

Lythe, M. B. and Vaughan, D. G.: BEDMAP: A New Ice Thickness and Subglacial Topographic Model of Antarctica, Journal of Geophysical

545   Research: Solid Earth, 106, 11 335–11 351, https://doi.org/10.1029/2000JB900449, 2001.

Maas, A. L., Hannun, A. Y., and Ng, A. Y.: Rectifier Nonlinearities Improve Neural Network Acoustic Models, in: ICML Workshop on Deep Learning for Audio, Speech, and Language Processing, 2013.

Markus, T., Neumann, T., Martino, A., Abdalati, W., Brunt, K., Csatho, B., Farrell, S., Fricker, H., Gardner, A., Harding, D., Jasinski, M., Kwok, R., Magruder, L., Lubin, D., Luthcke, S., Morison, J., Nelson, R., Neuenschwander, A., Palm, S., Popescu, S., Shum, C., Schutz,

550   B. E., Smith, B., Yang, Y., and Zwally, J.: The Ice, Cloud, and Land Elevation Satellite-2 (ICESat-2): Science Requirements, Concept, and Implementation, Remote Sensing of Environment, 190, 260–273, https://doi.org/10.1016/j.rse.2016.12.029, 2017.

Masi, G., Cozzolino, D., Verdoliva, L., and Scarpa, G.: Pansharpening by Convolutional Neural Networks, Remote Sensing, 8, 594, https://doi.org/10.3390/rs8070594, 2016.

Monnier, J. and Zhu, J.: Inference of the Bed Topography in Poorly Flew over Ice-Sheets Areas from Surface Data and a Reduced Uncertainty

555   Flow Model, 2018.

Morlighem, M.: MEaSUREs BedMachine Antarctica, Version 1, https://doi.org/10.5067/C2GFER6PTOS4, 2019.

Morlighem, M., Rignot, E., Seroussi, H., Larour, E., Ben Dhia, H., and Aubry, D.: A Mass Conservation Approach for Mapping Glacier Ice Thickness: BALANCE THICKNESS, Geophysical Research Letters, 38, n/a–n/a, https://doi.org/10.1029/2011GL048659, 2011.

Morlighem, M., Williams, C. N., Rignot, E., An, L., Arndt, J. E., Bamber, J. L., Catania, G., Chauché, N., Dowdeswell, J. A., Dorschel,

560   B., Fenty, I., Hogan, K., Howat, I., Hubbard, A., Jakobsson, M., Jordan, T. M., Kjeldsen, K. K., Millan, R., Mayer, L., Mouginot, J., Noël, B. P. Y., O'Cofaigh, C., Palmer, S., Rysgaard, S., Seroussi, H., Siegert, M. J., Slabon, P., Straneo, F., van den Broeke, M. R., Weinrebe, W., Wood, M., and Zinglersen, K. B.: BedMachine v3: Complete Bed Topography and Ocean Bathymetry Mapping of Greenland From Multibeam Echo Sounding Combined With Mass Conservation, Geophysical Research Letters, 44, 11,051–11,061, https://doi.org/10.1002/2017GL074954, 2017.

565   Morlighem, M., Rignot, E., Binder, T., Blankenship, D., Drews, R., Eagles, G., Eisen, O., Ferraccioli, F., Forsberg, R., Fretwell, P., Goel, V., Greenbaum, J. S., Gudmundsson, H., Guo, J., Helm, V., Hofstede, C., Howat, I., Humbert, A., Jokat, W., Karlsson, N. B., Lee, W. S., Matsuoka, K., Millan, R., Mouginot, J., Paden, J., Pattyn, F., Roberts, J., Rosier, S., Ruppel, A., Seroussi, H., Smith, E. C., Steinhage, D., Sun, B., van den Broeke, M. R., van Ommen, T. D., van Wessem, M., and Young, D. A.: Deep Glacial Troughs and Stabilizing Ridges Unveiled beneath the Margins of the Antarctic Ice Sheet, Nature Geoscience, https://doi.org/10.1038/s41561-019-0510-8, 2019.

570   Mouginot, J., Rignot, E., and Scheuchl, B.: Continent-Wide, Interferometric SAR Phase, Mapping of Antarctic Ice Velocity, Geophysical Research Letters, 46, 9710–9718, https://doi.org/10.1029/2019GL083826, 2019a.

Mouginot, J., Rignot, E., and Scheuchl, B.: MEaSUREs Phase Map of Antarctic Ice Velocity, Version 1, https://doi.org/10.5067/PZ3NJ5RXRH10, 2019b.

Nasrollahi, K. and Moeslund, T. B.: Super-Resolution: A Comprehensive Survey, Machine Vision and Applications, 25, 1423–1468,

575   https://doi.org/10.1007/s00138-014-0623-4, 2014.

Nias, I. J., Cornford, S. L., and Payne, A. J.: Contrasting the Modelled Sensitivity of the Amundsen Sea Embayment Ice Streams, Journal of Glaciology, 62, 552–562, https://doi.org/10.1017/jog.2016.40, 2016.

Park, T., Liu, M.-Y., Wang, T.-C., and Zhu, J.-Y.: Semantic Image Synthesis with Spatially-Adaptive Normalization, arXiv:1903.07291 [cs], 2019.

580 Raymond, M. J. and Gudmundsson, G. H.: On the Relationship between Surface and Basal Properties on Glaciers, Ice Sheets, and Ice Streams, Journal of Geophysical Research: Solid Earth, 110, https://doi.org/10.1029/2005JB003681, 2005.

Rippin, D., Bingham, R., Jordan, T., Wright, A., Ross, N., Corr, H., Ferraccioli, F., Le Brocq, A., Rose, K., and Siegert, M.: Basal Roughness of the Institute and Möller Ice Streams, West Antarctica: Process Determination and Landscape Interpretation, Geomorphology, 214, 139–147, https://doi.org/10.1016/j.geomorph.2014.01.021, 2014.

585 Robin, G. D. Q., Swithinbank, C., and Smith, B.: Radio Echo Exploration of the Antarctic Ice Sheet, in: International Symposium on Antarctic Glaciological Exploration (ISAGE), edited by Gow, A., Keeler, C., Langway, C., and Weeks, W., no. 86 in IASH Publication, pp. 97–115, International Association of Scientific Hydrology, Hanover, New Hampshire, USA, 1970.

Rumelhart, D. E., Hinton, G. E., and Williams, R. J.: Learning Representations by Back-Propagating Errors, Nature, 323, 533–536, https://doi.org/10.1038/323533a0, 1986.

590 Scambos, T.: Snow Megadune, pp. 1–3, Springer New York, New York, NY, https://doi.org/10.1007/978-1-4614-9213-9_620-1, 2014.

Scarpa, G., Vitale, S., and Cozzolino, D.: Target-Adaptive CNN-Based Pansharpening, IEEE Transactions on Geoscience and Remote Sensing, 56, 5443–5457, https://doi.org/10.1109/TGRS.2018.2817393, 2018.

Sergienko, O. V. and Hindmarsh, R. C. A.: Regular Patterns in Frictional Resistance of Ice-Stream Beds Seen by Surface Data Inversion, Science, 342, 1086–1089, https://doi.org/10.1126/science.1243903, 2013.

595 Shi, L., Allen, C. T., Ledford, J. R., Rodriguez-Morales, F., Blake, W. A., Panzer, B. G., Prokopiack, S. C., Leuschen, C. J., and Gogineni, S.: Multichannel Coherent Radar Depth Sounder for NASA Operation Ice Bridge, in: 2010 IEEE International Geoscience and Remote Sensing Symposium, pp. 1729–1732, IEEE, Honolulu, HI, USA, https://doi.org/10.1109/IGARSS.2010.5649518, 2010.

Siegert, M. J., Taylor, J., Payne, A. J., and Hubbard, B.: Macro-Scale Bed Roughness of the Siple Coast Ice Streams in West Antarctica, Earth Surface Processes and Landforms, 29, 1591–1596, https://doi.org/10.1002/esp.1100, 2004.

600 Simonyan, K. and Zisserman, A.: Very Deep Convolutional Networks for Large-Scale Image Recognition, arXiv:1409.1556 [cs], 2014.

Solheim, A. and Louise Pfirman, S.: Sea-Floor Morphology Outside a Grounded, Surging Glacier; Bråsvellbreen, Svalbard, Marine Geology, 65, 127–143, https://doi.org/10.1016/0025-3227(85)90050-7, 1985.

The IMBIE team: Mass Balance of the Antarctic Ice Sheet from 1992 to 2017, Nature, 558, 219–222, https://doi.org/10.1038/s41586-018-0179-y, 2018.

605 Tokui, S., Yamazaki Vincent, H., Okuta, R., Akiba, T., Niitani, Y., Ogawa, T., Saito, S., Suzuki, S., Uenishi, K., and Vogel, B.: Chainer: A Deep Learning Framework for Accelerating the Research Cycle, in: Proceedings of the 25th ACM SIGKDD International Conference on Knowledge Discovery & Data Mining - KDD '19, pp. 2002–2011, ACM Press, Anchorage, AK, USA, https://doi.org/10.1145/3292500.3330756, 2019.

Tsai, R. and Huang, T. S.: Multiframe Image Restoration and Registration, in: Advance Computer Visual and Image Processing, edited by
610 Huang, T. S., vol. 1, pp. 317–339, JAI Press, Greenwich, CT, 1984.

van Pelt, W. J. J., Oerlemans, J., Reijmer, C. H., Pettersson, R., Pohjola, V. A., Isaksson, E., and Divine, D.: An Iterative Inverse Method to Estimate Basal Topography and Initialize Ice Flow Models, The Cryosphere, 7, 987–1006, https://doi.org/10.5194/tc-7-987-2013, 2013.

Wang, X., Yu, K., Wu, S., Gu, J., Liu, Y., Dong, C., Loy, C. C., Qiao, Y., and Tang, X.: ESRGAN: Enhanced Super-Resolution Generative Adversarial Networks, arXiv:1809.00219 [cs], 2018.

615 Wang, Z., Bovik, A., Sheikh, H., and Simoncelli, E.: Image Quality Assessment: From Error Visibility to Structural Similarity, IEEE Transactions on Image Processing, 13, 600–612, https://doi.org/10.1109/TIP.2003.819861, 2004.

Wessel, P., Luis, J., Uieda, L., Scharroo, R., Wobbe, F., Smith, W., and Tian, D.: The Generic Mapping Tools Version 6, Geochemistry, Geophysics, Geosystems, https://doi.org/10.1029/2019GC008515, 2019.

Xu, Z., Wang, X., Chen, Z., Xiong, D., Ding, M., and Hou, W.: Nonlocal Similarity Based DEM Super Resolution, ISPRS Journal of Photogrammetry and Remote Sensing, 110, 48–54, https://doi.org/10.1016/j.isprsjprs.2015.10.009, 2015.

Yang, J., Fu, X., Hu, Y., Huang, Y., Ding, X., and Paisley, J.: PanNet: A Deep Network Architecture for Pan-Sharpening, in: 2017 IEEE International Conference on Computer Vision (ICCV), pp. 1753–1761, IEEE, Venice, https://doi.org/10.1109/ICCV.2017.193, 2017.

Yang, W., Zhang, X., Tian, Y., Wang, W., and Xue, J.-H.: Deep Learning for Single Image Super-Resolution: A Brief Review, arXiv:1808.03344 [cs], 2018.

620